

Potentially Underestimated Gas Flaring Activities - A New Approach to Detect Combustion Using Machine Learning and NASA's Black Marble Product Suite

Srija Chakraborty¹, Tomohiro Oda^{1,2,3}, Virginia L. Kalb⁴, Zhuosen Wang^{4,5}, Miguel O. Román⁶

1 Earth from Space Institute, Universities Space Research Association, Columbia, MD, US

2 Department of Atmospheric and Oceanic Science, University of Maryland, College Park, MD, US

3 Graduate School of Engineering, Osaka University, Suita, Osaka, Japan

4 Terrestrial Information Systems Laboratory, NASA Goddard Space Flight Center, Greenbelt, MD, US

5 Earth System Science Interdisciplinary Center, University of Maryland, College Park, MD, US

6 Leidos Civil Group, Integrated Missions Operation, Reston, VA, US

Abstract

Monitoring changes in greenhouse gas (GHG) emission is critical for assessing climate mitigation efforts towards the Paris Agreement goal. A crucial aspect of science-based GHG monitoring is to provide objective information for quality assurance and uncertainty assessment of the reported emissions. Emission estimates from combustion events (gas flaring and biomass burning) are often calculated based on activity data (AD) from satellite observations, such as those detected from the Visible Infrared Imaging Radiometer Suite (VIIRS) onboard the Suomi-NPP and NOAA-20 satellites. These estimates are often incorporated into carbon models for calculating emissions and removals. Consequently, errors and uncertainties associated with AD propagate into these models and impact emission estimates. Deriving uncertainty of AD is therefore crucial for transparency of emission estimates but remains a challenge due to the lack of evaluation data or alternate estimates. This work proposes a new approach using machine learning (ML) for combustion detection from NASA's Black Marble product suite and explores the assessment of potential uncertainties through comparison with existing datasets. We jointly characterize combustion using thermal and light emission signals, with the latter improving detection of probable weaker combustion with less distinct thermal signatures. Being methodologically independent, the differences in ML-derived estimates with existing approaches can indicate the potential uncertainties in detection. The approach was applied to detect gas flaring activities over the Eagle Ford Shale, Texas. We analyzed the spatio-temporal variations in detections and found that approximately 79.04% and 72.14% of the light emission-based detections are missed by ML-derived detections from VIIRS thermal bands and existing datasets, respectively. The region was impacted by the winter storm Uri which resulted in a significant reduction of flaring activities followed by a post-storm resumption. Our method is extendible to combustion events, such as biomass and waste burning, and can be scaled globally for transparent emission estimate reporting.

Keywords: NASA Black Marble, gas flaring, anomaly detection

1. Introduction

Monitoring changes in greenhouse gas (GHG) emissions and resulting levels of atmospheric carbon dioxide (CO₂) is critical for assessing climate mitigation effort towards the 1.5°C goal under the Paris Climate Agreement (<https://www.un.org/en/climatechange/paris-agreement>). The science research community has developed novel approaches to detect atmospheric CO₂ changes for climate monitoring by utilizing observations and modeling (e.g. Weir et al. 2021; Zeng et al. 2021).

From among a variety of carbon emission sources, emissions from combustion are relatively uncertain compared to other emissions from the energy sector, although these are calculated from the same bottom-up approach (IPCC 2006) as

Emissions = Activity data (AD) x Emission Factor (EF).

For CO₂ from fossil fuel combustion, AD and EF for the energy sector are highly constrained for the system boundary (IPCC 2006; Oda et al. 2021a). AD for energy production is also reported with high precision (5% 2 sigma reported uncertainty) for fuel consumed. On the other hand, AD for combustion events, such as gas flares and biomass burning, are often based on estimates (e.g., gas flare, fire counts) and the total fuel amount consumed within the system. Moreover, EF for biomass burning is highly uncertain (Akagi et al. 2011), while EF for fossil fuels is uncertain unless the chemical composition is known. Combustion emissions are incorporated in carbon modeling for estimating emissions and removals (Crowell et al. 2019) causing errors and uncertainties from combustion events to potentially alias final emission estimates. Reducing these errors is crucial for maturing carbon monitoring systems (CMS), especially ones based on atmospheric inversions (Oda et al. 2019, 2021b).

A challenge for evaluating emissions from combustion is the lack of fiducial reference data, particularly with gridded emission estimate reports (Andres et al. 2016, Oda et al. 2018, 2019). This has been tackled by intercomparing emission estimates and using differences as a proxy for errors and uncertainties (Oda et al. 2015, 2018, 2019, Andres et al. 2016, Pan et al. 2019). As these differences are attributable to underlying computation and datasets used, intercomparisons allow the characterization of emission differences and its drivers (Oda et al. 2019, Pan et al. 2019). This contributes to quality assurance and uncertainty analysis recommended by the IPCC guidelines and is essential for robust and transparent emission reporting. When the methodologies and underlying datasets are shared by different estimates, the process of assigning and propagating uncertainties is often iterative in nature and is generally not performed systematically. For example, satellite-derived estimates of fire emissions are often based on AD from sensors such as the Visible Infrared Imaging Radiometer Suite (VIIRS) (Justice et al., 2013). This is exacerbated in cases where detections from one dataset solely, such as VIIRS Nightfire (VNF) (Elvidge et al. 2013, 2019), is used as the primary basis for gas flaring estimates.

This study proposes a machine learning (ML) approach for detecting combustion by utilizing VIIRS thermal band and nighttime light (NTL) observations from NASA's Black Marble product suite (VNP46, Román et al. 2018) by jointly characterizing its day/night visible and thermal emission. The approach is data-driven, and methodologically independent of existing techniques, such as the VNF algorithm, and leverages the orthogonal information embedded in VIIRS observations. Most importantly, our approach *generates an independent detection set and can be used to assess uncertainty in VIIRS-derived combustion estimates*. We applied the approach for gas flare detection in the Eagle Ford Shale, Texas, US, explored the role of light emission signals in improving detection, and examined the differences with legacy methods (VNF) to generate a potential detection uncertainty.

2 Combustion Detection

2.1 Gas flare detection

While the global share is less than 1 % of the total fossil fuel emissions (Gilfillan et al. 2021), flaring associated with oil and natural gas production contributes to regional and local GHG and air pollution emissions with severe impacts on the environment and Earth's climate (Allen et al. 2013, Zhang et al. 2019, Caseiro et al. 2019, Fisher and Wooster 2019, Faruolo et al. 2020, Cushing et al. 2021). Monitoring these events is essential for tracking adherence to mitigation policies, such as Zero Routine Flaring by 2030 (The World Bank, 2019) and progress towards the Paris Climate Agreement Goal (IPCC 2006, Falkner 2016, Zhang et al. 2019).

Daily nighttime satellite observations are used for detecting combustion from flaring and fires on a global scale. These approaches commonly utilize the VIIRS thermal bands for detection (Csiszar et al. 2014, Schroeder et al. 2014, Schroeder and Giglio 2018, Elvidge et al. 2013, 2019, Zhang et al. 2015, Liu et al. 2018, Lu et al. 2020, Zhizhin et al. 2021). Flares detected by VNF (Elvidge et al. 2013, 2019) have been used to assess resulting emissions and its environmental impact (Deetz and Vogel 2017, Zhang et al. 2019,

Sun et al. 2020, Franklin et al. 2019, Cushing et al. 2021). VNF has also been utilized for determining and mapping gas flare emissions in a widely used gridded inventory (Janssens-Maenhout et al. 2019), leaving scope for errors and uncertainties in VNF to impact such derived analysis.

2.2 Proposed Methodology

Table 1: VNP46A1 Dataset

Dataset	Bands	Wavelength (μm)	Emission Signal
VNP46A1 15 arc second, daily (Román et al. 2018)	DNB	0.5-0.9	Light
	M-10	1.58-1.64	Thermal
	M-11	2.23-2.28	
	M-12	3.61-3.79	
	M-13	3.97-4.93	
	M-15	10.26-11.26	
	M-16	11.54-12.49	

We propose an anomaly detection approach utilizing the top-of-atmosphere Day/Night Band (DNB) and moderate band (M-band) observations from Black Marble VNP46A1 to characterize the anomalous light and thermal emission of flares. Table 1 shows the VNP46A1 dataset consisting of a set of M-bands and the DNB acquired by the VIIRS instrument. We derive a high confidence set with both thermal and light response, a moderate confidence urban-masked, light-only response set, which are merged to derive daily detections.

Increased adoption of ML in combustion and emission monitoring has been observed to detect power plant activities from visible images (Couture et al. 2020), emissions from combustion (Finch et al. 2022), and fire using thermal bands (Wang et al. 2021a). We explore its applicability in extracting multispectral thermal and light emission properties of VIIRS-based combustion. Although DNB has improved flare and fire detection (Polivka et al. 2016, Elvidge et al. 2019), it is used as a confirmatory feature only, while nightlight-only images have been used to detect offshore drilling (Lu et al. 2020, Wang et al. 2021b). The DNB lies in the visible/Near-Infrared region and has a large dynamic range (0.5 to 0.9 μm) that captures the light emission from combustion. The DNB is sensitive to weaker anomalies, especially with a small source area (Elvidge et al. 2019), and allows fire phase estimation (Wang et al. 2020). We also include light-emission-only signals from the DNB and examine its role in enabling weak combustion detection.

Our approach is based on learning a multispectral model of the non-anomalous thermal and light signal of the background and monitoring subsequent observations for deviations (See SI: Methodology). As flares cause high thermal and light emissions, these deviations show pixel-based anomaly scores. The models are learned from a small volume of data from the region. The study duration consists of $K = 38$ observations that are divided for training $D_T = [X_1, X_2, \dots, X_t]$ to learn background models, and test $D_a = [X_{t+1}, X_{t+2}, \dots, X_K]$, when the trained models are applied to new observations. X_k is a multispectral image where pixel i forms $x_{k,i} \in X_k$, a 7-dimensional vector $x_{k,i} = [x_{k,i}^M, x_{k,i}^{DNB}]$, with M representing all M-bands. D_T is divided into training and validation subsets, with the former used for learning background distribution and the latter used for hyperparameter tuning.

Training and Validation:

M-band background model (Thermal Emission): We characterize the non-anomalous multispectral thermal (M-10 to M-16) properties of the background using an autoencoder (Hinton and Salakhutdinov 2006; Baldi 2012) by training it on clear M-band spectra from the training subset. Anomalies in the validation subset are detected from the deviation of a pixel’s spectra from the autoencoder’s reconstruction and denoted as anomaly score. As thermal emissions have a high response in M-10 and M-11, we also apply the Reed-Xiaoli (RX) detector (Chang and Chiang 2002) and learn the background distribution in these

bands to detect anomalies from the deviation from daily background statistics. These approaches jointly model thermal bands and reduce single-band spurious detections.

DNB Background Model (Light Emission): We characterize the DNB background signal to analyze a pixel's deviation and factor in its immediate spatial neighbors to detect light emission. We partition the scene radiance from the training subset into clusters using a Gaussian mixture model (GMM). For each cluster, we derive a spatial relationship that predicts the central pixel's radiance as a function of its spatial neighbors using an elastic net (Zou and Hastie, 2005). In the validation subset, the trained GMM assigns each pixel to a cluster, and the elastic net is applied to its neighbors to determine its high radiance likelihood or anomaly score using a daily variance-based threshold.

Both M-band and DNB are impacted by clouds and require masking. The standard VIIRS cloud mask (VNP35) (Kopp et al. 2014) is known to mislabel nighttime clouds (Wang et al. 2021c) and flags thermal anomalies as 'cloudy' (Elvidge et al. 2013). To minimize these errors, we train a cloud model from M-12 to M-16 using principal component analysis (PCA) to project the spectra onto a 2-D space and learn the distance at which cloudy pixels lie from the projection median. For new observations, we apply the PCA model and assign cloud labels based on a pixel's proximity to training day cloud projections. Cloudy pixels with high thermal anomaly scores are flagged as contaminations. During high lunar illumination, clouds contaminate DNB while light emission may appear through clouds. We apply the anomalous light-emission detector over clouds, which sets clouds as background to remove such contaminations but retains anomalous DNB radiance appearing through clouds.

Test:

We apply the trained models to the dataset as shown in Figure 1 to detect thermal and light anomalies. We predict cloud labels by applying PCA-distancing on each pixel. The detectors are then applied to extract candidate anomalies. The thermal anomalies are obtained from autoencoder and RX deviations, with thresholds determined from daily variance. High anomaly scores form the detected set after removal of cloud and water pixels. We compute the DNB anomaly score, identify pixels exceeding the daily threshold and suppress visible clouds under high lunar illumination. We then use per-pixel urban settlement information from World Settlement Footprint (WSF) (Marconcini et al. 2020) and retain pixels with no urban signal to obtain anomalous light emissions.

Detection Sets: The anomalous thermal and light emissions are utilized to form the daily combined, DNB-only, and joint detection sets as shown in Figure 1. The *combined set* consists of pixels with both anomalous thermal and light emissions. Anomalous light emissions are filtered further to increase decision confidence by retaining pixels i) that lie in a neighborhood with negligible WSF score, and ii) with at least one band (M-10 to M-13) deviating positively above the background to minimize interference from unlikely combustion signals, such as electric lighting. This forms the *DNB-only set* capturing anomalous light emission, including those from weaker anomalies with less distinct thermal signals. The *joint detection set* consists of total detections from combined and DNB-only sets.

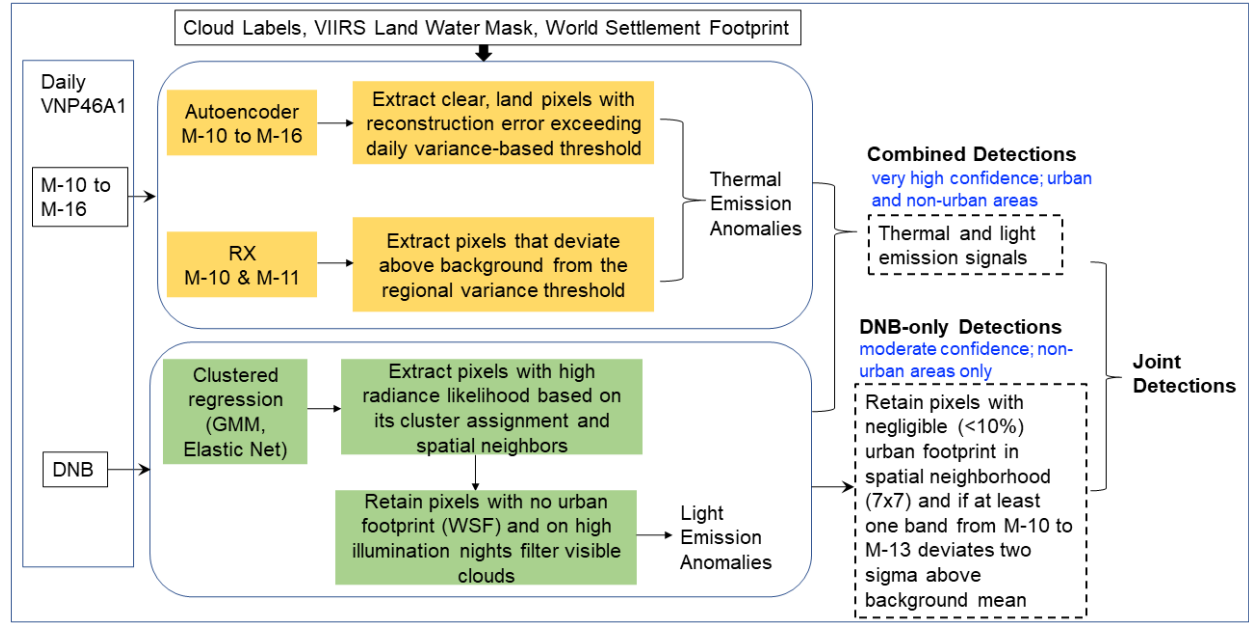


Figure 1: Workflow of proposed flaring detection from VNP46A1 and derived detection sets.

2.3 Experimental Details

We applied the detectors over the densely-welled Eagle Ford Shale (Wolaver et al. 2018, boundary from EIA) to assess detection performance. Our study area (26.9375N to 29.8542N and -97.0167W to -99.9394W) corresponds to a 700x700 gridded block during 01/22/2021–02/28/2021 with 12 observations in the training set (See SI: Experimental details). The duration was selected to encompass the lunar cycle and examine performance under varying lunar illumination and cloud cover. This also includes the winter storm Uri that affected natural gas production (Doss-Gollin et al. 2021) and allows assessment of flaring activity variations.

3. Results

3.1 Evaluating and interpreting detections

The average number of anomalies detected by the methods under clear and cloudy conditions is shown in Figure 2, with the DNB-only set detecting approximately four times more anomalous pixels than the combined set. The increased detection with DNB can be attributed to its higher sensitivity to light emission from weaker thermal anomalies over clear and cloudy nights during all lunar cycle phases. As the spatial extent of flaring signal can vary between M-bands and DNB, we consider the combined method to have matched a DNB-only detection, if there is at least one combined detection within a 3x3 grid centering a DNB-only detection. We found that $79.04 \pm 2.23\%$ of the DNB-only detections were missed by the combined method. We examine the nature of DNB-only and combined detections in the next sections.

The lack of ground truth combustion data hinders validation, especially for the DNB-only detections, which lack confirmation from thermal bands. Accurate flare labeling in the DNB is infeasible by experts given its spatial footprint and daily variation. This is further compounded by cloud contamination under high lunar illumination, DNB signal leakage around urban areas (Wang et al. 2021c), and unsuppressed features in the WSF layer. We assessed the likelihood of the detections being associated with flares and flaring sites by contrasting the multispectral signal of detections with the background and examining visible features in higher resolution imagery after removing contaminations from false positives (FP). We calculated the fraction of FP as $n(FP)/n(\text{pixels in the area})$, where $n(\cdot)$ is the number of pixels. For $n(FP)$ we outline the errors due to unremoved visible clouds and urban leakage around cities using LabelMe (Kentaro 2016). Throughout the study duration, this fraction is 0.00282 ± 0.00101 , and

0.0117±0.002 in the block and Eagle Ford area respectively, while no FP were observed in the combined set. Thus, contaminations are negligible due to the use of daily variance-based thresholds and masking and show the detectors' potential at monitoring daily combustion activity.

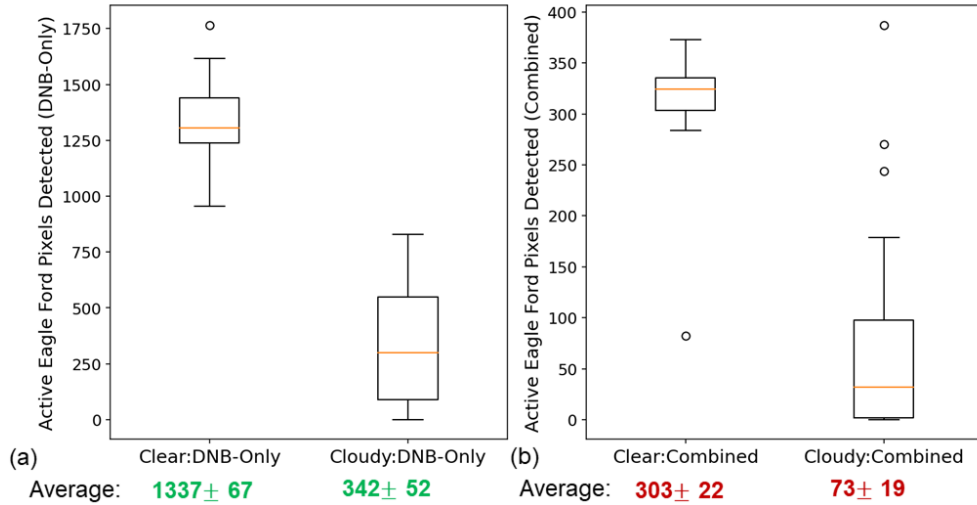


Figure 2: Average number of detections during the study period in Eagle Ford using the (a) DNB-only and (b) combined methods during clear and cloudy nights.

The detections were analyzed using the following approaches:

Multispectral profile: We calculated the ratio of the average signal from the detections to that from the background in each band as shown in Table 2 (See Table SI-2). This ratio (and difference in M-12 and M-13) is high in each band for the combined detections, *indicating these are very likely anomalies*. The DNB-only detections showed a high deviation from background in DNB, M-10, and M-11. The higher M-10 and M-11 signals of the DNB-only set, where gas flaring peaks indicate that these detections are *likely thermal anomalies* that are relatively weaker than combined detections.

Table 2: Ratio of Clear Night Detection Signal against the Background in the Eagle Ford area.

Detection, Bands	DNB	M-10	M-11	M-12 (difference (K))	M-13 (difference (K))
DNB-only	13.04	222	119.16	1.003 (0.89)	1.002 (0.59)
Combined	48.09	1055.4	150.55	1.011 (3.01)	1.005 (1.3)

Co-location with flaring sites: We compared the spatio-temporal aggregate of the detections over the Eagle Ford area with indicators of flaring infrastructure to examine their co-location. We resampled an openly available flaring well dataset of the region from 2015 from The Texas Railroad Commission, (ArcGIS) to 15 arc seconds. At least one flaring site was found in a 7x7 grid centering 73.92%, 71.04%, and 74.91% of the DNB-only, combined, and VNF detections respectively, indicating that VIIRS-derived estimates showed comparable co-location with the well dataset. We also compared the DNB-only detections with a regional Landsat-8 composite (Gorelick et al. 2017) and confirmed by visual analysis that well pads are co-located with our detections (Figure 3 a, b, and c). On examining the DNB-only and combined detections non-co-located with the well dataset, we observed 74.61% and 89.22% of the detections overlap with these

visible features in the composite, respectively. The increased co-location with well pads is likely due to the composite's acquisition dates matching closely with the study duration. Although ground truth combustion information is unavailable, high co-location indicates that *DNB-only detections are associated with flaring sites and minimally contaminated by non-flaring sites*. Here, we selected the minimum grid size that also makes the co-location analysis feasible.

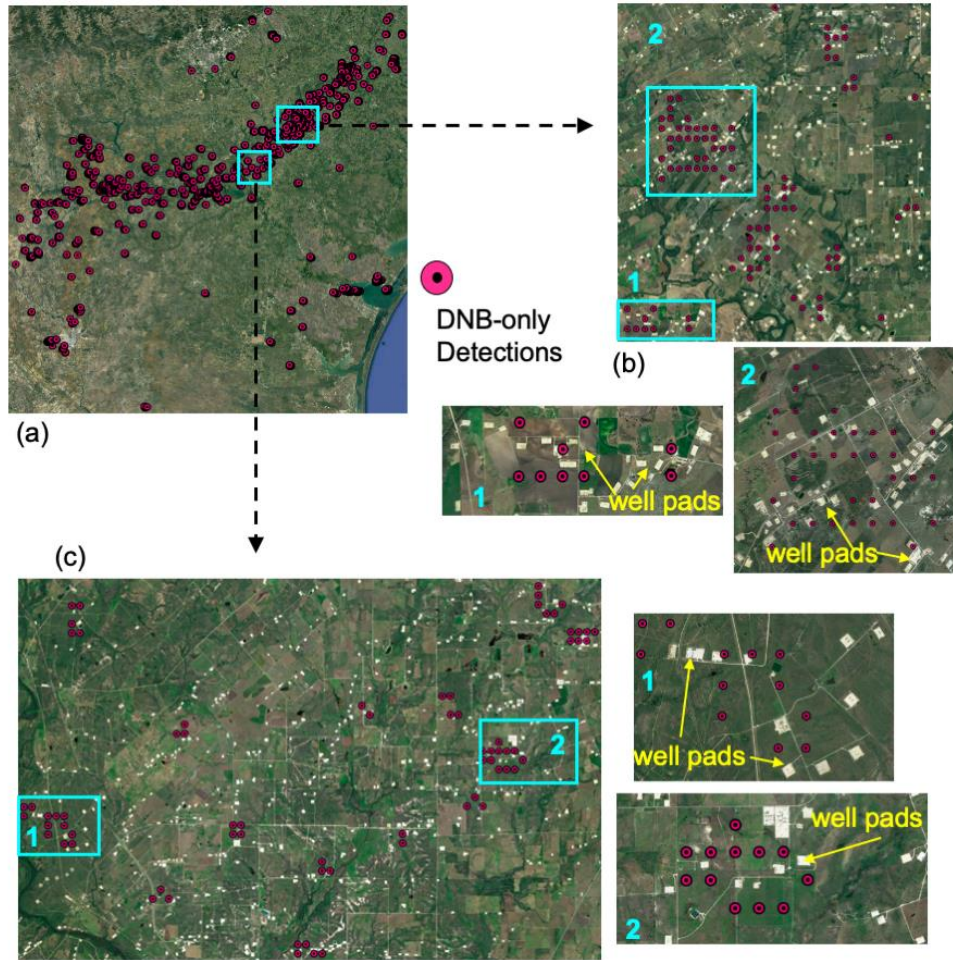


Figure 3: a) Aggregate of DNB-only detections over the study area. b) and c) shows examples of the light emission-only detections co-located with visible well pads in a Landsat-8 composite.

This indicates that DNB-only detections have weaker thermal signals and are probable flares missed by the thermal bands, while the combined set consists of high confidence detections. The sets together capture possible daily flaring activity at emission sites and provide a more accurate representation of flaring.

We examined the degree of flaring activity persistence by comparing the detections with the annual Black Marble product suite NTL product (VNP46A4) from 2020. Persistence indicates consistent gas flaring and is important for monitoring changes at these sites. We observe $62.47 \pm 0.32\%$ and $82.43 \pm 0.34\%$ overlap between DNB-only and combined detections with the composite, showing persistent flaring at these locations.

3.2. Comparison with VNF

We compare our daily detections (ML_k) with VNF (VNF_k) to evaluate the overlap and increase in detection from the ML-based multispectral interpretation of flaring. For a VNF detection, a larger number of adjacent pixels are detected by the methods. If we observe at least one detection within a 5X5 grid centering a VNF detection, such flares are considered to have overlapped. This is expressed as $o = (VNF_k \cap ML_k) / |VNF_k|$.

We observe comparable overlap between VNF and the proposed approaches as shown in Table 3, showing that the methods *effectively extract flaring signatures*. The combined detections overlap with confirmed VNF detections. Approximately 87.0648% of the non-overlaps correspond to non-confirmed VNF events, which may include spurious detections. DNB-only detections show an increased overlap with VNF. The joint set shows a high overlap with VNF. We found four observations with ML detections that are missed by VNF, and overlap is thus reported for 34 observations. Unlike VNF detections where M-bands are separately analyzed, the autoencoder and RX jointly learn a multispectral distribution of the M-bands. This lowers the chance of spurious detections in the combined set that are seen in confirmed (A2021057) and non-confirmed (A2021041) VNF detections.

ML-enabled detections that do not appear in VNF are indicated through detections missed by VNF as

$$d_m = (ML_k \setminus VNF_k) / |ML_k|.$$

We compute d_m for pixels in ML_k for which at least one detection is not recorded in VNF_k within a 5x5 grid centering the ML detection. Table 3 lists all metrics showing *increased detection with ML_k* . For the DNB-only set d_m is computed over detections that overlap with well pads in the Landsat composite. We hand-label persistent DNB detection locations that do not show spatial overlap with visible well-pads in Landsat imagery to exclude such detections and these have been masked to the best of our knowledge. The *inclusion of urban-masked DNB as a feature extracts weak thermal anomalies and lowers the detection threshold without increasing FP errors*.

Table 3: Comparison of Proposed Approaches with VNF

Detection (ML_k), Metric	o (%)	d_m (%)
Combined	74.74 ± 3.19 , *96.73	16.70 ± 3.32
DNB-only	78.67 ± 3.65	72.14 ± 4.16
Joint	90.5 ± 2.83	67.94 ± 3.53

*compared with confirmed VNF detections.

3.3. Temporal Variation in Gas Flaring Activity

Figure 4 shows daily detection counts from the methods and VNF. Winter storm Uri, (Day of Year 44, 2021- 48, 2021) reduced natural gas production in the region (Doss-Gollin et al. 2021) and corresponds to reduced DNB-only and combined detections. The reduction observed even in the DNB, which is more sensitive to weaker or cloud-obscured flares, indicates a possible reduction in flaring activity. Minimum activity is observed on February 15, 2021 and is lower than the expected detection levels under cloudy conditions noted during earlier phases. This may be caused by clouds (signal attenuation) and reduction in flaring activity. The number of active pixels increases at the end of this phase showing recovery to pre-storm flaring levels. All methods show similar flaring trends throughout the study duration.

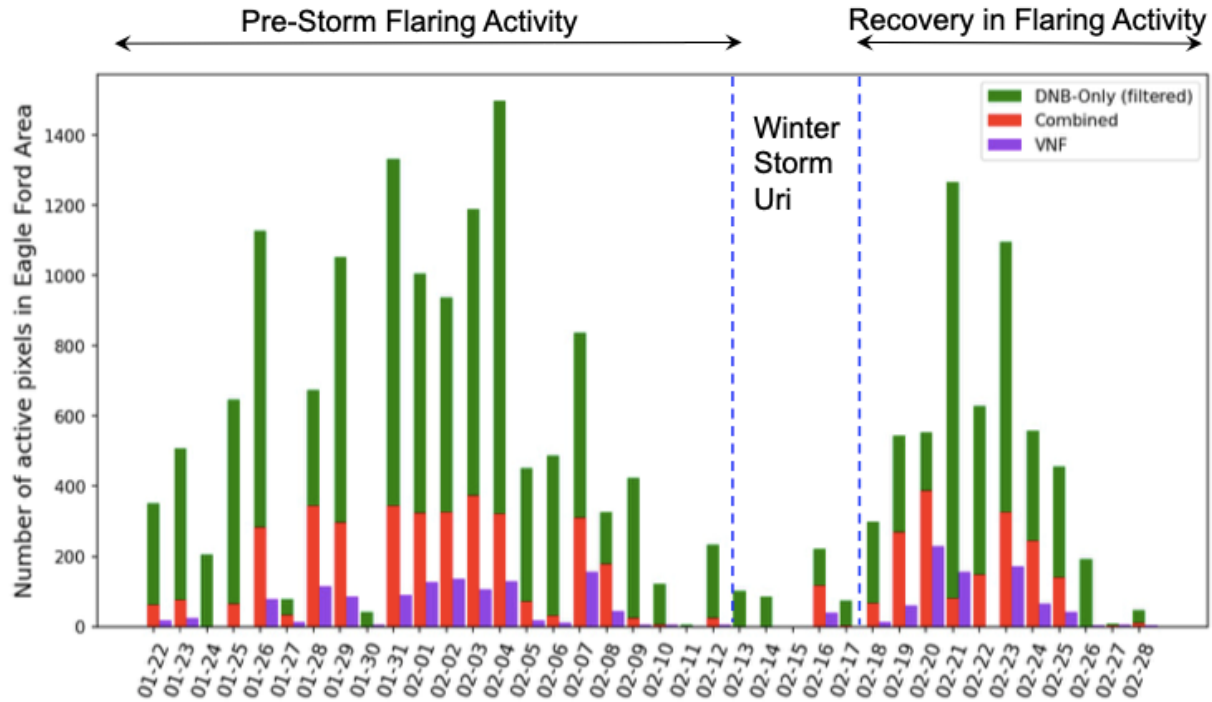


Figure 4. Detections in the Eagle Ford area using combined and DNB-only (filtered implies overlapping combined detections are removed) sets and VNF. Reduction in detections is caused by clouds, while the sustained drop from Feb 13, 2021 is associated with thick cloud cover and reduction in flaring.

3.4 Impact of VIIRS-Derived Estimates of Flaring Activity

The proposed method is expected to impact VIIRS-derived flaring estimates. Figure 5 compares the binarized average clear night spatio-temporal distribution of flaring between the detection sets, with DNB improving the spatial distribution and temporal persistence estimates as seen from detection intensities.

Independently derived estimates can allow intercomparison of datasets to assess detection error. Figure 6 (a) and (b) shows the binarized average clear night spatio-temporal distribution of flaring from ML-based detections and VNF. Figure 6 (c) highlights the difference in both spatial distribution and temporal persistence of flaring activity, with approximately 72% of the difference arising from light emission. Given the lack of complete validation of VIIRS-derived flares, intercomparison of detections can allow assessment of potential uncertainty in existing gridded emission maps such as Emissions Database for Global Atmospheric Research (EDGAR) (Janssens-Maenhout et al. 2019).

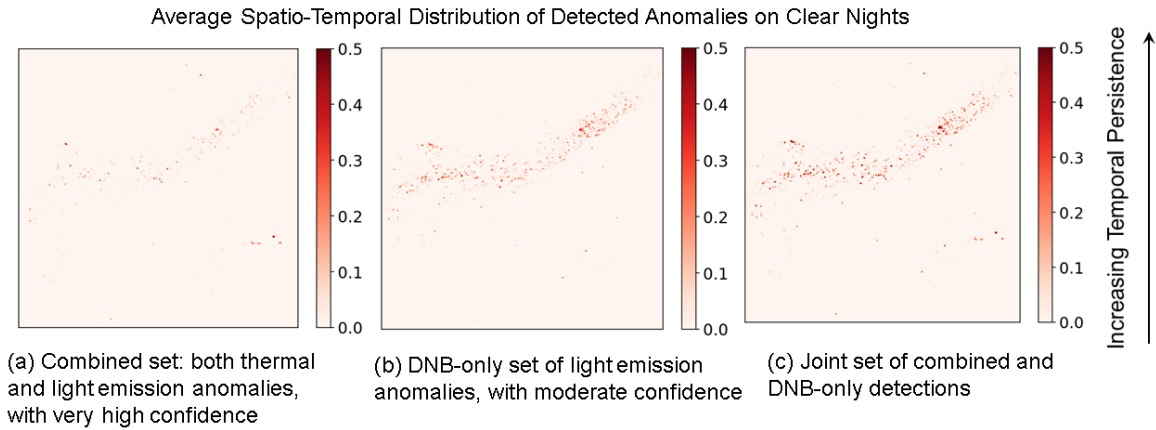


Figure 5. Average spatial distribution and temporal persistence of flaring from a) combined, b) DNB-only, and (c) joint sets at 30 arc second, showing the improvement due to DNB signal, which is expected to enhance combustion attribution (spatial) and tracking (temporal).

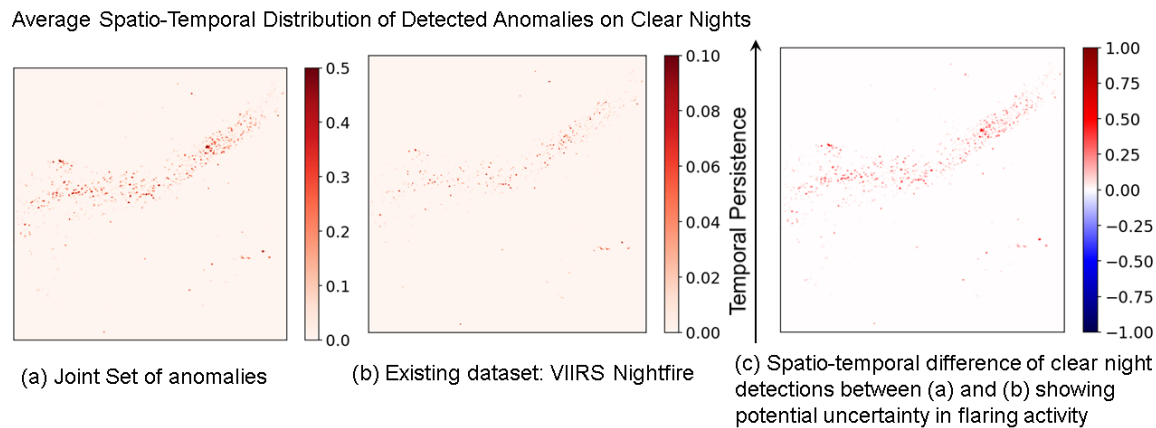


Figure 6. Average spatial distribution and temporal persistence of flaring from a) proposed approach, b) VNF at 30 arc second, and c) difference signal between (a) and (b).

4. Discussion

Our proposed approach improves nighttime flare detection by jointly considering all VNP46A1 bands and the urban-masked DNB-only signal, *allowing detection of likely weaker anomalies*. The approach consistently captures a more accurate representation of daily flaring and is expected to improve attribution and tracking of emission-causing activity. We also created an *independent, data-driven methodology* to detect flares. Although an estimate, the difference of the detections with existing datasets can highlight detection error and uncertainty as demonstrated.

This study shares the limitation of the lack of evaluation data with other studies and highlights the need for collecting evaluation data for improving the accuracy of estimates. A limitation of the light-emission-only set is that its co-occurrence with non-flaring light signals, such as electric lighting, cannot be decoupled. However, retaining urban-masked DNB-only detections with positive deviation from the background in at least one M-band minimizes the scope of such contaminations in the detections. The performance is also dependent on ancillary layers such as the WSF and the cloud mask.

Our approach is agnostic to combustion type and can be extended to detect biomass and waste burning. Biomass burning emissions are prescribed in carbon flux inversions, and the differences among estimates should have a significant impact on carbon flux estimation, especially, the estimation of carbon removals. The IPCC guideline uses burned area estimates from satellite-derived AD and requires quality assurance

and uncertainty analysis that is currently unreported. Our approach should allow localizing sources of uncertainties in AD and examining errors in model representation and computation.

Lastly, we note that this is a step towards multifaceted Black Marble-based emission mapping that is ideally suited for CMS studies, given its extensive quality and uncertainty assessment (Wang et al. 2021c). NTL-derived estimates of human-caused emission (Oda and Maksyutov 2011, Oda et al. 2018) and city-level CO₂ emissions have been improved by leveraging Black Marble (Oda et al. 2021b). Being a physical measurement, satellite-derived NTL can create derived, value-added carbon products with science traceability through error and uncertainty estimates.

5. Conclusion

This study proposed and developed a machine learning-based nighttime gas flare detector using NASA's Black Marble product suite by jointly modeling the thermal and light emission signals. Our approach generates an independent flaring activity estimate and provides an opportunity for assessing uncertainty associated with VIIRS-based flaring estimates through comparison with existing combustion datasets. We applied the detector over the Eagle Ford Shale and showed the urban-masked light emission signal to be sensitive to probable weak flares and should improve its detection compared to thermal bands. Our approach is agnostic to combustion type and is extendible to events such as biomass and waste burning. Future studies will explore generalization techniques to scale our approach globally for contributing to transparent emission reporting.

Data availability statement

The datasets are available through NASA's official Level-1 and Atmosphere Archive and Distribution System. Experimental code and labels are available upon request.

Acknowledgment

The authors would like to thank Dr. Eleanor C. Stokes (EfSI, USRA) for reviewing this manuscript. S. Chakraborty's research was supported by an appointment to the NASA Postdoctoral Program at the Goddard Space Flight Center, administered by Universities Space Research Association under contract with NASA. The authors acknowledge the support from NASA's Terra, Aqua, Suomi-NPP, and NOAA-20 program under the NASA grant 80NSSC22K0199 for the Black Marble Product.

References:

- Akagi S K, Yokelson R J, Wiedinmyer C, Alvarado M J, Reid J S, Karl T, Crounse J D and Wennberg P O 2011 Emission factors for open and domestic biomass burning for use in atmospheric models *Atmospheric Chemistry and Physics* **11**(9) 4039-4072
- Allen D T, Torres V M, Thomas J, Sullivan D W, Harrison M, Hendler A, Herndon S C, Kolb C E, Fraser M P, Hill A D and Lamb B K 2013 Measurements of methane emissions at natural gas production sites in the United States *Proceedings of the National Academy of Sciences* **110**(44) 17768-17773
- Alvarez R A, Pacala S W, Winebrake J J, Chameides WL and Hamburg S P 2012 Greater focus needed on methane leakage from natural gas infrastructure *Proceedings of the National Academy of Sciences* **109**(17) 6435-6440
- Andres R J, Boden T A and Higdon D M 2016 Gridded uncertainty in fossil fuel carbon dioxide emission maps, a CDIAC example *Atmospheric Chemistry and Physics* **16**(23) pp.14979-14995
- ArcGIS
<https://www.arcgis.com/apps/Cascade/index.html?appid=627f465609664172a07a45995cc5e155> (last access: March 9, 2022)
- Baldi P 2012 Autoencoders, unsupervised learning, and deep architectures. In *Proceedings of ICML Workshop on unsupervised and transfer learning* JMLR Workshop and Conference Proceedings, 37-49

Caseiro A, Gehrke B, Rücker G, Leimbach D and Kaiser J W 2019 Gas flaring activity and black carbon emissions in 2017 derived from Sentinel-3A SLSTR *Earth Syst. Sci. Data Discuss* **10**

Chang C I and Chiang S S 2002 Anomaly detection and classification for hyperspectral imagery *IEEE Transactions on Geoscience and Remote Sensing* **40**(6) 1314-1325

Couture H, O'Connor J, Mitchell G, Söldner-Rembold I, D'souza D, Karra K, Zhang K, Kargar A R, Kassel T, Goldman B and Tyrrell D 2020 Towards tracking the emissions of every power plant on the planet *NeurIPS Workshop* **3**

Crowell S, Baker D, Schuh A, Basu S, Jacobson A R, Chevallier F, Liu J, Deng F, Feng L, McKain K and Chatterjee A 2019 The 2015–2016 carbon cycle as seen from OCO-2 and the global in situ network *Atmospheric Chemistry and Physics* **19**(15) 9797-9831

Csiszar I, Schroeder W, Giglio L, Ellicott E, Vadrevu K P, Justice C O and Wind B 2014 Active fires from the Suomi NPP visible infrared imaging radiometer suite: Product status and first evaluation results *Journal of Geophysical Research: Atmospheres* **119** (2) 803–816

Cushing L J, Chau K, Franklin M and Johnston J E 2021 Up in smoke: characterizing the population exposed to flaring from unconventional oil and gas development in the contiguous US *Environmental Research Letters* **16**(3) 034032

Doss-Gollin J, Farnham D J, Lall U and Modi V 2021 How unprecedented was the February 2021 Texas cold snap? *Environmental Research Letters* **16**(6) 064056

Deetz K and Vogel B 2017 Development of a new gas-flaring emission dataset for southern West Africa *Geoscientific Model Development* **10**(4) 1607-1620

EIA, U.S. Energy Information Administration, <https://atlas.eia.gov/datasets/major-tight-oil-and-shale-gas-play-eagle-ford-play-extent/explore> (last access: Mar 10, 2022)

Elvidge C D, Zhizhin M, Hsu F C and Baugh KE 2013 VIIRS Nightfire: Satellite pyrometry at night *Remote Sensing* **5**(9) 4423-4449

Elvidge C D, Zhizhin M, Baugh K, Hsu F C and Ghosh T 2019 Extending nighttime combustion source detection limits with short wavelength VIIRS data *Remote Sensing* **11**(4) 395

Everhart K and Molnar G 2021 Severe power cuts in Texas highlight energy security risks related to extreme weather events *IEA Paris. February*

Faruolo M, Caseiro A, Lacava T and Kaiser J W 2020 Gas Flaring: A Review Focused on Its Analysis from Space *IEEE Geoscience and Remote Sensing Magazine* **9**(1) 258-281

Falkner R 2016 The Paris agreement and the new logic of international climate politics *International Affairs* **92**(5) 1107–1125

Fisher D and Wooster M J 2019 Multi-decade global gas flaring change inventoried using the ATSR-1, ATSR-2, AATSR and SLSTR data records *Remote Sensing of Environment* **232** 111298

Finch D P, Palmer P I and Zhang T 2022 Automated detection of atmospheric NO₂ plumes from satellite data: a tool to help infer anthropogenic combustion emissions *Atmospheric Measurement Techniques* **15**(3) 721-733

Franklin M, Chau K, Cushing L J and Johnston J E 2019 Characterizing flaring from unconventional oil and gas operations in south Texas using satellite observations *Environmental science & technology* **53**(4) 2220-2228

Gilfillan D, Marland G, Boden T, Andres R 2021 Global, Regional, and National Fossil-Fuel CO₂ Emissions 1751-2018 CDIAC-FF, Research Institute for Environment, Energy, and Economics, Appalachian State University.

Gorelick N, Hancher M, Dixon M, Ilyushchenko S, Thau D and Moore R 2017 Google Earth Engine: Planetary-scale geospatial analysis for everyone *Remote sensing of Environment* **202** 18-27

Hinton G E and Salakhutdinov R R 2006 Reducing the dimensionality of data with neural networks *Science*, **313**(5786) 504-507

IPCC 2006 2006 IPCC Guidelines for National Greenhouse Gas Inventories Prepared by the National 38 Greenhouse Gas Inventories Programme ed H S Eggleston et al (Hayama: the Institute for Global 39 Environmental Strategies (IGES))

Janssens-Maenhout G, Crippa M, Guizzardi D, Muntean M, Schaaf E, Dentener F, Bergamaschi P, Pagliari V, Olivier J G J, Peters J A H W, van Aardenne J A, Monni S, Doering U, Petrescu A M R, Solazzo E and Oreggioni G D 2019 EDGAR v4.3.2 Global Atlas of the three major greenhouse gas emissions for the period 1970–2012 *Earth Syst. Sci. Data* **11** 959–1002

Justice C O, Román M O, Csiszar I, Vermote E F, Wolfe R E, Hook S J, Friedl M, Wang Z, Schaaf C B, Miura T and Tschudi M 2013 Land and cryosphere products from Suomi NPP VIIRS: Overview and status. *Journal of Geophysical Research: Atmospheres*, **118**(17) 9753-9765

Kentaro W 2016 LabelMe: Image Polygonal Annotation with Python <https://github.com/wkentaro/labelme> (last access: March 11, 2022)

Kopp T J, Thomas W, Heidinger A K, Botambekov D, Frey R A, Hutchison K D, Iisager B D, Brueske K and Reed B 2014 The VIIRS Cloud Mask: Progress in the first year of S-NPP toward a common cloud detection scheme *Journal of Geophysical Research: Atmospheres* **119**(5) 2441-2456

Liu Y, Hu C, Zhan W, Sun C, Murch B and Ma L 2018 Identifying industrial heat sources using time-series of the VIIRS Nightfire product with an object-oriented approach *Remote Sensing of Environment* **204** 347-365

Lu W, Liu Y, Wang J, Xu W, Wu W, Liu Y, Zhao B, Li H and Li P 2020 Global proliferation of offshore gas flaring areas *Journal of Maps* **16**(2) 396-404

Marconcini M, Metz-Marconcini A, Üreyen S, Palacios-Lopez D, Hanke W, Bachofer F, Zeidler J, Esch T, Gorelick N, Kakarla A and Paganini M 2020 Outlining where humans live, the World Settlement Footprint 2015 *Scientific Data* **7**(1) 1-14

Oda T and Maksyutov S 2011 A very high-resolution (1 km×1 km) global fossil fuel CO₂ emission inventory derived using a point source database and satellite observations of nighttime lights *Atmospheric Chemistry and Physics* **11**(2) 543-556

Oda T, Ott L, Topylko P, Halushchak M, Bun R, Lesiv M, Danylo O and Horabik-Pyzel J 2015 Uncertainty associated with fossil fuel carbon dioxide (CO₂) gridded emission datasets

Oda T, Maksyutov S and Andres R J 2018 The Open-source Data Inventory for Anthropogenic CO₂, version 2016 (ODIAC2016): a global monthly fossil fuel CO₂ gridded emissions data product for tracer transport simulations and surface flux inversions *Earth System Science Data* **10**(1) 87-107

Oda T, Bun R, Kinakh V, Topylko P, Halushchak M, Marland G, Lauvaux T, Jonas M, Maksyutov S, Nahorski Z and Lesiv M 2019 Errors and uncertainties in a gridded carbon dioxide emissions inventory *Mitigation and Adaptation Strategies for Global Change* **24**(6) 1007-1050

Oda T, Haga C, Hosomi K, Matsui T and Bun R 2021a Errors and uncertainties associated with the use of unconventional activity data for estimating CO₂ emissions: the case for traffic emissions in Japan. *Environmental Research Letters*, **16**(8) 084058

Oda T, Román M O, Wang Z, Stokes E C, Sun Q, Shrestha R M, Feng S, Lauvaux T, Bun R, Maksyutov S, Chakraborty S, Paynter I and Kalb V L 2021b US Cities in the Dark: Mapping Man-Made Carbon Dioxide Emissions Over the Contiguous US Using NASA's Black Marble Nighttime Lights Product. *Urban Remote Sensing: Monitoring, Synthesis, and Modeling in the Urban Environment* 337-367

Pan X, Ichoku C, Chin M, Bian H, Darmentov A, Colarco P, Ellison L, Kucsera T, da Silva A, Wang J and Oda T 2020 Six global biomass burning emission datasets: intercomparison and application in one global aerosol model *Atmospheric Chemistry and Physics* **20**(2) 969-994

Polivka T N, Wang J, Ellison L T, Hyer E J and Ichoku C M 2016 Improving nocturnal fire detection with the VIIRS Day–Night band *IEEE Transactions on Geoscience and Remote Sensing* **54**(9) 5503-5519

Reed I S and Yu X 1990 Adaptive multiband c-far detection of an optical pattern with unknown spectral distribution *IEEE Transaction on Acoustic, Speech, Signal Processing* (**38**) 1760-1770

Román M O, Wang Z, Sun Q, Kalb V, Miller S D, Molthan A, Schultz L, Bell J, Stokes E C, Pandey B and Seto K C 2018 NASA's Black Marble nighttime lights product suite *Remote Sensing of Environment* **210** 113-143

Schroeder W, Oliva P, Giglio L and Csiszar I A 2014 The New VIIRS 375 m active fire detection data product: Algorithm description and initial assessment *Remote Sensing of Environment* **143** 85-96

- Schroeder W and Giglio L 2018 NASA VIIRS Land Science Investigator Processing System (SIPS) Visible Infrared Imaging Radiometer Suite (VIIRS) 375 m & 750 m Active Fire Products: product User's Guide Version 1.4. Product User's Guide Version 1
- Sun S, Li L, Wu Z, Gautam A, Li J and Zhao W 2020 Variation of industrial air pollution emissions based on VIIRS thermal anomaly data *Atmospheric Research* **244** 105021.
- The World Bank Zero Routine Flaring by 2030 <https://www.worldbank.org/en/programs/zero-routine-flaring-by-2030> (last access: March 11, 2022)
- Wang J, Roudini S, Hyer E J, Xu X, Zhou M, Garcia L C, Reid J S, Peterson D A and da Silva A M 2020 Detecting nighttime fire combustion phase by hybrid application of visible and infrared radiation from Suomi NPP VIIRS *Remote Sensing of Environment* **237** 111466
- Wang Y, Ni Y, Li X and Ye Y 2021a A Deep Learning Approach To Nightfire Detection Based On Low-Light Satellite
- Wang Q, Wu W, Su F, Xiao H, Wu Y and Yao G 2021b Offshore Hydrocarbon Exploitation Observations from VIIRS NTL Images: Analyzing the Intensity Changes and Development Trends in the South China Sea from 2012 to 2019 *Remote Sensing* **13**(5) 946
- Wang Z, Román M O, Kalb V L, Miller S D, Zhang J and Shrestha R M 2021c Quantifying uncertainties in nighttime light retrievals from Suomi-NPP and NOAA-20 VIIRS Day/Night Band data *Remote Sensing of Environment* **263** 112557
- Weir B, Crisp D, O'Dell C W, Basu S, Chatterjee A, Kolassa J, Oda T, Pawson S, Poulter B, Zhang Z and Ciais P 2021 Regional impacts of COVID-19 on carbon dioxide detected worldwide from space *Science Advances* **7**(45) eabf9415
- Wolaver B D, Pierre J P, Labay B J, LaDuc T J, Duran C M, Ryberg W A and Hibbitts T J 2018 An approach for evaluating changes in land-use from energy sprawl and other anthropogenic activities with implications for biotic resource management *Environmental earth sciences* **77**(5) 1-14
- Zeng N, Han P, Liu Z, Liu D, Oda T, Martin C, Liu Z, Yao B, Sun W, Wang P and Cai Q 2021 Global to local impacts on atmospheric CO₂ from the COVID-19 lockdown, biosphere and weather variabilities *Environmental Research Letters* **17**(1) 015003
- Zhang X, Scheving B, Shoghli B, Zygarlicke C and Wocken C 2015 Quantifying gas flaring CH₄ consumption using VIIRS *Remote Sensing* **7**(8) 9529-9541
- Zhang Y, Gautam R, Zavala-Araiza D, Jacob D J, Zhang R, Zhu L, Sheng J X and Scarpelli T 2019 Satellite-observed changes in Mexico's offshore gas flaring activity linked to oil/gas regulations. *Geophysical Research Letters* **46**(3) 1879-1888
- Zhizhin M, Matveev A, Ghosh T, Hsu F C, Howells M and Elvidge C 2021 Measuring Gas Flaring in Russia with Multispectral VIIRS Nightfire *Remote Sensing* **13**(16) 3078
- Zou H and Hastie T 2005 Regularization and variable selection via the elastic net *Journal of the Royal Statistical Society: Series B (Statistical Methodology)* **67**(2) 301-320

Supplementary Information

Methodology:

Autoencoder: The background model is learned from the non-anomalous pixel-level brightness temperature, $x_{k,i}^M$ from cloud-free observations in the training subset by minimizing multispectral reconstruction error. This is applied on the validation subset to detect pixel deviations of the input with its reconstruction $\hat{x}_{k,i}^M$ as $A(x_{k,i}^M) = |x_{k,i}^M - \hat{x}_{k,i}^M|$, where $A(\cdot)$ is the anomaly score.

RX: For the RX detector the anomaly score in M-10 and M-11 11 (M') bands are obtained using $A(x_{k,i}^{M'}) = (x_{k,i}^{M'} - \mu_k^{M'})^T \Sigma_k^{-1} (x_{k,i}^{M'} - \mu_k^{M'})$. Here $\mu_k^{M'}$ and Σ_k^{-1} are derived from the daily observations and describe the background.

Anomalous Light Emission Detector (DNB): A Gaussian mixture model divides the scene from the training subset D_t into C clusters from selected cloudy and clear observations. Elastic nets are trained on each cluster that predicts the central pixel radiance x_i^{DNB} as a function of its neighbors x_n , as $x_i^{DNB} = w_{0,c} + \sum_n w_{n,c} x_n$, where $W_c: w_{n,c}$ represents the regression coefficients of cluster C over a 3x3 neighborhood. In the validation subset, clustering assigns each pixel x_i^{DNB} into a radiance cluster C . The final high radiance prediction of this pixel, \hat{x}_i^{DNB} is obtained by applying its cluster regression weights on its neighbors $\hat{x}_i^{DNB} = W_{n,c} x_{k,n}$. High radiance pixels are detected using $A(x_{k,i}^{DNB}): \hat{x}_i^{DNB} > \tau_k^{DNB}$.

Cloud: We learn the cloud model from M-12 to M-16 by deriving the principal components by projecting each pixel in D_t to a 2-D space to obtain the projections $p(x_{t,i})$. The Manhattan distance $d(p(x_{t,i}), m_t)$ of the pixel projections from the projection median m_t is computed. We then use LabelMe to outline the clouds and form a one-class model describing the eigenspace distance of cloudy pixels. The distance is compared against a threshold τ^C to derive labels cloudy when $d_{cloudy}(\cdot) < \tau^C$ and clear when $d(\cdot) > \tau^C$.

For anomaly decision making, the following tests are performed:

- a) Autoencoder: $A(x_{k,i}^{M'}) > \tau_k^M$, where $\tau_k^M = \mu(A(x_{k,i}^M)) + c^M \sigma(A(x_{k,i}^M))$, $c^M=2$. Before computing τ_k^M , we retain $x_{k,i}^M$ if it is a clear land pixel with less than 5% cloud cover within a 7x7 spatial grid.
- b) RX: $A(x_{k,i}^{M'}) > \tau^{M'}$, where $\tau^{M'} = \mu(A(x_{t,i}^{M'})) + c^{M'} \sigma(A(x_{t,i}^{M'}))$, $c^{M'}=1$
- c) DNB: $A(x_{k,i}^{DNB}): \hat{x}_{k,i}^{DNB} > \tau_k^{DNB}$, where $\tau_k^{DNB} = \mu(A(\hat{x}_{k,i}^{DNB})) + l \cdot \sigma(A(\hat{x}_{k,i}^{DNB}))$, $l=0.5$. For filtering clouds, the same test is performed with $l=2$ over cloudy pixels on nights with lunar illumination higher than 10%. To get DNB-only detections, we create a binarized WSF mask WSF_{net} , and derive the net urban response across a local grid and retain anomalous pixels that are with negligibly impacted by urban signal from neighboring pixels. This is done by retaining x_i when $x_{WSF-net,i} < 10\%$ in a 7x7 grid and at least one band in M-10 to M-13 is two standard deviations above the background mean.
- d) Clouds: $d(p(x_{t,i}^{Mc}), m_t) < \tau^C$, where $\tau^C = \mu(d(p(x_{t,i}^{Mc}), m_t)) + 1.5\sigma(d(p(x_{t,i}^{Mc}), m_t))$.

Here $\mu(\cdot)$ and $\sigma(\cdot)$ implies mean and standard deviation. $c^M, c^{M'}, l, \tau^C$ are determined from validation subset.

The anomaly score is indicative of the degree of anomaly and its maxima can be used to localize flares.

Experimental Details:

The autoencoder model is trained on a 200 x 200 block in the study area, while the RX and DNB models are trained across the study area (700 x 700 pixel block). The autoencoder is trained over 100 epochs, with a batch size of 512 using exponential linear unit activations and Adam optimization over 40000x2 pixels by minimizing the mean absolute error loss with 20% of the data as the validation subset.

Autoencoder layers:

Encoder: Input (6), Dense (8), Dense (4), Dense (2);

Decoder: Dense (4), Dense (8), Dense (6): Reconstruction

Each layer is l2 regularized to reduce overfitting.

The DNB cluster number is determined from Akaike Information criterion and set to 5. For the elastic net we set $\alpha=1$, $l1$ -ratio=0.3.

D_T consists of 12 (A2021022-A2021033) observations and we select a subset of observations for training (Table SI-1) and the rest are used in the validation subset.

Table SI-1: Training Subsets

Method	Training set observations
Autoencoder	A2021032 (clear), A2021033 (clear)
RX	A2021022, A2021024, A2021031, A2021032
DNB	A2021022 (almost clear), A2021023 (almost clear), A2021031 (clear)

Table SI-2: Clear Night DNB-only and Combined Detection Signal with respect to Background in the Eagle Ford area.

Bands, Detection Set	Active DNB-only	Active Combined	Background DNB-only	Background Combined
DNB (nWcm ⁻² sr ⁻¹)	46.55±4.11	186.12±17.65	3.57 ± 0.56	3.87 ± 0.55
M-10 (Wm ⁻² m ⁻¹ sr ⁻¹)	4.44 x 10 ⁻² ± 0.0161	9.52 x 10 ⁻² ± 0.01	-2 x 10 ⁻⁴ ± 0.001	9.02 x 10 ⁻⁵ ± 0.001
M-11 (Wm ⁻² m ⁻¹ sr ⁻¹)	2.3832 x 10 ⁻² ± 0.0074	6.82 x10 ⁻² ±0.0074	2 x 10 ⁻⁴ ± 0.0004	4.53 x 10 ⁻⁴ ± 0.0004
M-12 (K)	279.91±0.78	282.03 ±0.71	279.02 ± 0.86	279.03 ± 0.86
M-13 (K)	277.36±0.62	278.07±0.59	276.77 ± 0.71	276.77 ± 0.71